AFTERBODY HEAT FLUX MEASUREMENTS IN THE NASA AMES HFFAF BALLISTIC RANGE

David W. Bogdanoff[*] and Michael C. Wilder[§]

[*]ERC Inc., NASA Ames Research Center, Moffett Field. CA 94035-1000;
[§]NASA Ames Research Center, Moffett Field. CA 94035-1000

Summary-In order to measure afterbody heat fluxes over a model in the ballistic range, the required modifications to a proven technique for measuring forebody heat fluxes are described. This involves the use of an extended helium gas plume to remove the glowing wake and the use of special high conductivity, high temperature capable graphite-filled plastic for the afterbody. The models and test conditions are described. Data in the form of plots of the surface temperature of the models are presented. Finally, experimental and computational fluid dynamic (CFD) heat flux data for forebody and afterbody heat fluxes are presented and compared. Data are presented for a 45 degree sphere-cone (with a projecting rear stud) at 2.70 km/s and for a sphere at 4.76 km/s. Both models were launched into 76 Torr of CO_2 gas. The experimental forebody heat fluxes were within 1.5% of the CFD values. The experimental afterbody heat fluxes were within 1% of the CFD values for the sphere, but only 51% of the CFD values for the sphere-cone.

I. INTRODUCTION

It is important to know the heat fluxes to be expected on the afterbodies of earth and planetary entry vehicles to allow the most efficient design of the afterbody heat shield. Improved afterbody heat flux data allows heat shield designs with smaller margins and hence, lower masses to be made. This, in turn, allows increased scientific payloads to be carried. Afterbody heat flux data, which is typically 3-6% of the stagnation point heat flux, [Ref. 1] are difficult to obtain. Data from wind tunnel tests can be seriously compromised by the presence of the sting and also, the free stream conditions, including the chemistry, are not exactly known. Also, there can be appreciable acoustic noise in the free stream, which can affect the flow over the test article. With the ballistic range technique there is no sting and the free stream is a known, quiescent condition. Established techniques for measuring the heat fluxes over the forebodies of entry vehicles will not work unmodified for the afterbody heat fluxes due to the strongly glowing wake and the weak thermal signature of the afterbodies.

This report begins with a review of the established techniques used for heat flux measurements on the forebodies of models in the NASA Ames HFFAF (hypervelocity free flight aerodynamics facility) ballistic range. The modifications of these techniques necessary to measure afterbody heat fluxes are then presented, along with preliminary experimental afterbody heat flux data.

The technique to measure the heat flux incident on the models in the ballistic range involves measuring the visible and infra-red (3 − 5 microns) emission from the model surface using calibrated cameras. Each camera takes a single frame picture of the model at some point in its flight down the range. Knowing the emissivity of the model surface, the model surface temperatures can be obtained. With the model surface temperature distribution known at several locations down the length of the range, the heat flux histories to the model surface can be calculated using the one-dimensional heat conduction equation. Further details of the technique are given in Ref. [2].

II. TEST FACILITY AND CAMERAS

Figure 1 shows a top view of the uprange end of the NASA Ames HFFAF ballistic range. The HFFAF is an enclosed, controlled-pressure aeroballistic range with a 22.9 meter-long test section over which 16 evenly spaced spark shadowgraph stations are distributed.   Only the first
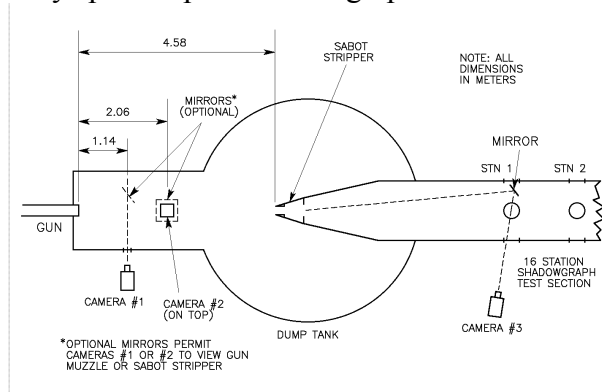

Figure 1. Top view of NASA Ames HFFAF ballistic range showing movie camera set-up.

two shadowgraph stations are shown in Fig. 1. Each station provides orthogonal side- and top-view shadowgraphs from which a projectile's 6 degrees-of-freedom (DOF) trajectory information – 3 position and 3 angle components – can be measured. Elapsed-time data, provided by 16 high-speed digital counters synchronized with the shadowgraphs, allow velocities and angular rates to be obtained from the measured trajectories. The HFFAF has a variety of launchers, which give it the capability to attain projectile velocities from the subsonic to the hypersonic regime.   A two stage light gas gun with a launch tube diameter of 3.81 cm was used for the present test campaign.   Figure 1 shows the locations of 3 digital movie cameras used to view launch package exit from the muzzle, sabot separation and model flight. At shadowgraph stations 3, 8 and 13, mid-wave infra-red (3 – 5 microns) FLIR/Indigo Phoenix (stations 3 and 8) or FLIR SC8000 (station 13) cameras are used to take 0.5 – 1.0 μs exposure near head-on photos of the models. Figure 2 shows a representative set-up for the infra-red cameras. A photo of a helium can (seen sketched in Fig. 2) is shown in Fig. 3. The can diameter is 20 cm.
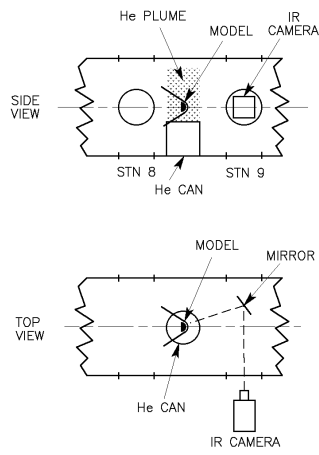

Figure 2. Representative set-up for the infra-red (IR) cameras. Model flies from left to right. A helium plume flowing out of the helium can is used to strip the glowing gas cap from the model so that the camera can measure only the emission from the model surface without confounding radiation from the gas cap. This allows the model surface temperatures and, hence, heat transfer rates to be determined.

Figure 3. Photo of representative helium can.

III. REPRESENTATIVE LAUNCH PACKAGES AND DATA
FOR FOREBODY HEAT FLUX MEASUREMENTS

Figure 4 shows a photo of a representative launch package for forebody heat flux measurements, with a section drawing shown in Fig. 5. The figures show the titanium sphere-cone model with a aluminum stud screwed into the aft end of the model. The model is sitting on 3 of the 4 serrated Nylon sabot fingers, which, in turn, are sitting on the polyethylene obturator cup. (The fourth sabot finger is seen off to the right in Fig. 4.)
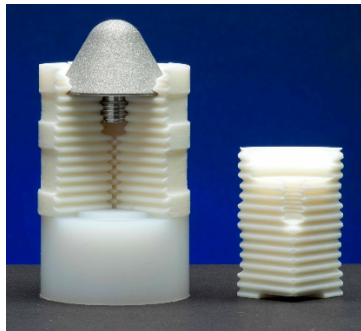

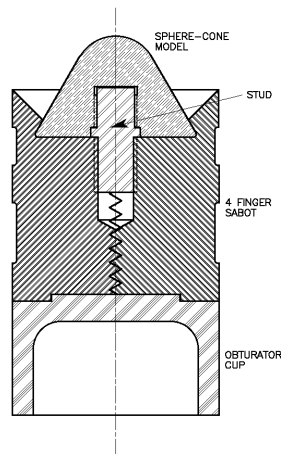Figure 4. Photo of representative launch package.

Figure 5. Section drawing of representative launch package.

Figure 6 shows a representative mid-wave (3 – 5 microns) infra-red photo taken mid-way down the range. The model is viewed from the front, with the camera looking from off to the side by roughly 20 degrees. The dark central region (on the spherical segment of the model) is with a relatively small model roughness height, whereas the bright annular region (on the cone) has a much larger roughness height and increased heat transfer and consequent higher temperature.
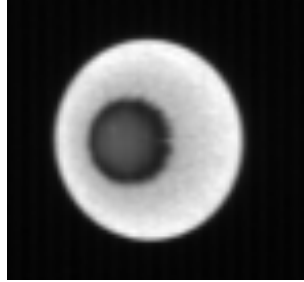

Figure 6. Infra-red (3 – 5 micron wavelength range) photo of sphere-cone model taken at station 8, midway down ballistic range. The model nose radius is 0.76 cm, velocity is 2.7 km/s, range is filled with CO_2 at a pressure of 76 Torr. Model is Ti-6Al-4V titanium alloy with a 45^0 cone angle and a diameter of 3.30 cm. Changes in model roughness account for the varying brightness (and temperature and heat flux) moving from the nose across the spherical section and down along the conical skirt of the model. Shot 2717.

Figure 7 below shows the heat flux at the gun muzzle for shot 2717. The muzzle heat flux was projected back from surface temperature data taken at stations 3 and 8. Model configuration and shot conditions are given in the caption of Figure 6. The calculated (CFD) heat flux at the stagnation point (s = 0) is 2342 W/cm^2, in fairly good agreement with the experimental value of 2250 W/cm^2. The CFD values were computed for axisymmetric models, laminar flow, a fully catalytic wall condition and with an 8 species chemistry model using the DPLR software {Ref. [3]}. As mentioned previously, away from the stagnation point roughness effects have major effects on the heat flux. The roughness height on the cone is about 3.4 times that on the spherical section and accounts for the much high heat flux on the cone.
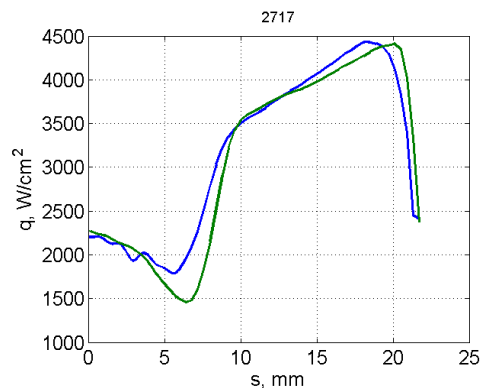

Figure 7. Heat fluxes at the gun muzzle for shot 2717. Based on wall temperature data at station 3 (blue line) and station 8 (green line). The green line corresponds to the photo of Fig. 6. s is the distance along the cone surface from the stagnation point.

IV. MODIFICATIONS OF FOREBODY HEAT FLUX MEASUREMENT TECHNIQUE FOR USE ON AFTERBODIES

The afterbody heat fluxes are estimated to be 3 – 6% of the stagnation point heat flux. To bring the temperature rises of the afterbody into the range of accessibility of the infrared cameras, one must use an afterbody material with low thermal conductivity compared to those of the 304 stainless steel and Ti-6Al-4V forebodies. Many plastics have relatively low thermal conductivities which could perhaps be suitable, but the majority of common plastics (e.g., ABS, acetal, acrylic, Nylon, polycarbonate) have limited temperature capability, and significant temperature rises (of the order of 250 C) would be required for the afterbody heat flux measurements. Poly-imides (e.g. DuPont Vespel) and poly-ether-ether-ketones (PEEK) have temperature capabilities of 260 – 360 C and would appear to be good candidates. Even with these high temperature capabilities, estimates of the plastic afterbody temperatures reached can exceed the capability of the plastics if unfilled plastics are used. However, versions of the plastics with 10 – 30 % of graphite or carbon fill have thermal conductivities 2.5 – 3 times higher than those of the unfilled plastics, which brings the estimated afterbody temperatures down to within the capabilities of the plastics. In addition, estimates of the infrared emissivities of the carbon or graphite filled plastics are near unity, which is very desirable. (The emissivities of the stainless steel and titanium range from 0.2 to 0.4, depending upon roughness.)

Three candidate plastics, listed in Table 1 below, were further investigated.

Table 1. Candidate afterbody plastics.

Plastic	Fill
Ensinger TECAPEEK PVX	30% carbon + graphite + Teflon
Quadrant EPP Ketron CM CA30 PEEK	30% carbon
DuPont Vespel SP-21 polyimide	15% graphite

At the temperature measurement location, it would be very desirable to have the plastic fill particles have dimensions less than the depth where the temperature difference from the wall temperature is, say, 5% of the difference between the wall temperature and the bulk temperature away from the wall. In such a case, we should be able to consider the conduction as fairly close to that of uniform material with average thermal properties of the plastic. This would not be the case if the fill particles were much larger, extending over a distance where the temperature differences reached, say, 50% of the difference between the wall temperature and the bulk temperature. From Ref. [4], for constant heat flux into a semi-infinite slab, the depth, y, where the temperature difference from the wall is 5% of the difference from the wall to the bulk material is given by

$$y = 0.1\sqrt{\alpha t} \qquad (1)$$

where:

α = thermal diffusivity
t = time from start of heat flux

The thermal diffusivity is given by

$$\alpha = \frac{k}{\rho C_p} \qquad (2)$$

where:

k = thermal conductivity
ρ = density
C_p = specific heat

The time, t, is given by

$$t = \frac{x}{u} \qquad (3)$$

where:

x = distance from gun muzzle to mid-range
u = model velocity

Combining Eqns. (1) – (3), we get

$$y = 0.1\sqrt{\frac{k}{\rho C_p}\frac{x}{u}} \qquad (4)$$

For the DuPont Vespel SP-21, k, ρ and C_p are available from data sheets, except that C_p is only given for the unfilled plastic. (We note here that the thermal properties of all three candidate plastics are very similar to each other.) A correction is made for C_p, using the known C_p for the 15% graphite fill. The correction is the mass fraction weighted sum of the C_p values for the unfilled plastic and for the fill. The distance from the gun muzzle to mid range, x, is 21.5 m. y was evaluated for two velocities covering the range of velocities used to date. These were 2.7 and 5.0 km/s. The corresponding depths, y, were 6.5 and 4.8 microns.

Figure 8 shows SEM micrographs of two of the three candidate plastics. For the TECAPEEK [(Fig. 8(a)], many fill pieces are 12 – 20 microns long and 7 to 8 microns in diameter. Also, in lower magnification micrographs (not shown), some fill pieces are seen to be 20 – 30 microns in diameter, with no smaller dimensions. The SEM micrograph for the Ketron PEEK was of poor quality due to charging issues and has many horizontal streak artifacts. For this reason, the micrograph is not shown here. However, the micrograph was sufficiently good to allow one to clearly see the dimensions of the fill particles. For the Ketron PEEK, fill pieces are 15 – 20 microns in diameter, with no smaller dimensions. For the Vespel [Fig. 8(b)], mostly the fill pieces are 8 – 20 microns long dimension, but 2 – 5 microns in diameter. Based on the smaller dimensions of the fill pieces for the Vespel, Vespel was selected as the plastic of choice.
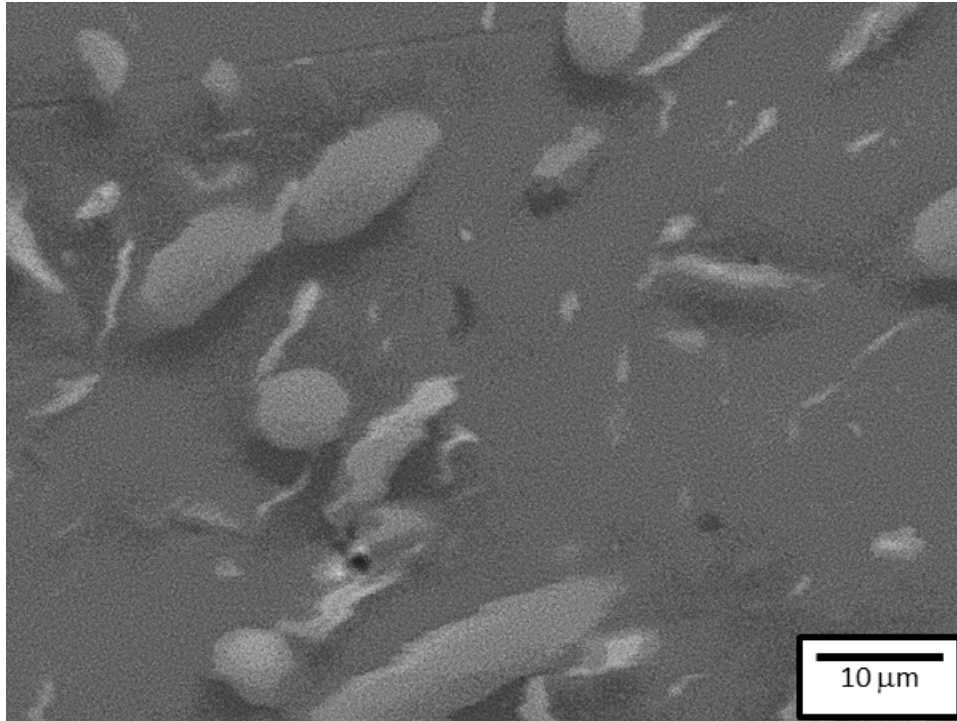
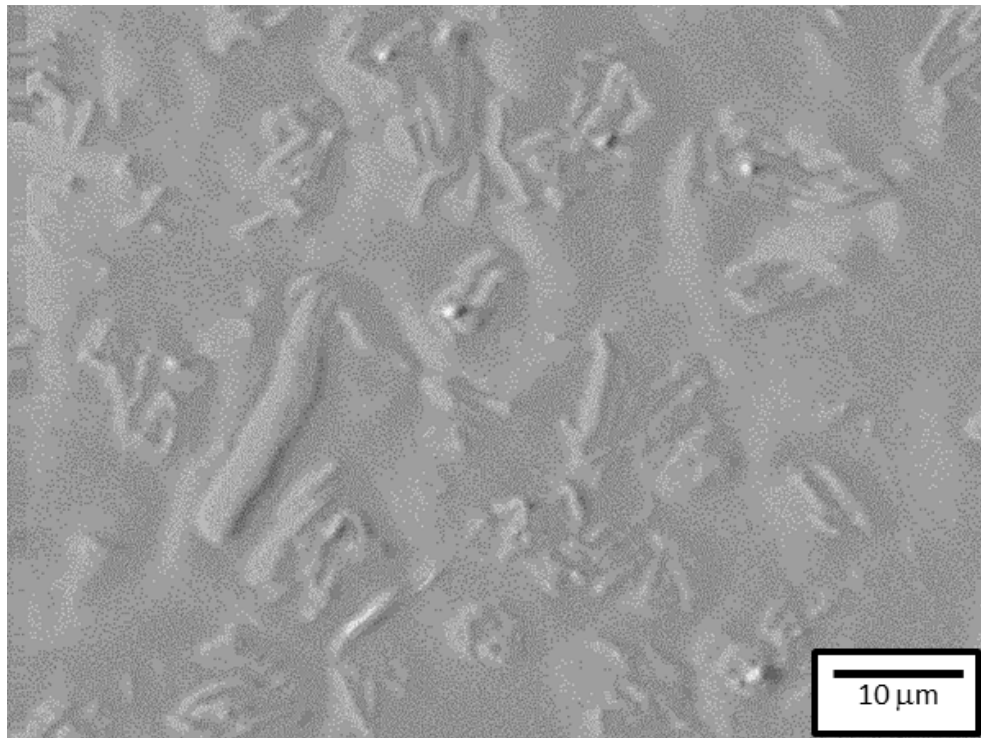Figure 8(a). SEM micrograph of Ensinger TECAPEEK PVX.

Figure 8(b). SEM micrograph of DuPont Vespel SP-21 polyimide.

In CO_2, the glowing wake is quite bright and can strongly interfere with measurements of the afterbody heat fluxes unless special measures are adopted. The glowing wake is removed by passing the model through a localized helium plume (typically 4x longer than for the forebody measurements). The high sound speed in helium results in much weaker aerodynamic quenching the radiation and allowing the model to separate from its luminous wake. Figures 9 and 10 show top views of three set-ups of the IR cameras and helium plume cans for the forebody and afterbody heat flux measurements. Figure 11 shows a photo of the helium plume cans, and can be compared with the single helium can used for the forebody heat flux measurements (Fig. 3).

The length of the helium plume for the afterbody measurements is four times the diameter of the plume used when only forebody measurements are being made. When the large area helium plume cans are used for afterbody heat flux measurements, care must be taken that excessive helium is not introduced into the test section. This may require reducing the pressures on the flow regulators supplying the helium plume cans. Excessive helium in the test section can be seen to produce kinks in the model shock waves seen in the shadowgraph pictures. When the helium plume flow is sufficiently low, the model shock waves should be well-shaped, without kinks, just like the shock waves seen when the helium plumes are not used.

When the model is flying in the helium plume, the heat flux will be much less than in the test gas (usually air or CO_2). This can actually cause the surface temperature of the model to decrease during the passage through the helium plume. In the one-dimensional heat flow analysis to relate experimentally observed model surface temperature to heat flux in the test gas, the reduction of heat flux in the helium must be taken into account. The method for doing this is given in Sec. VII.
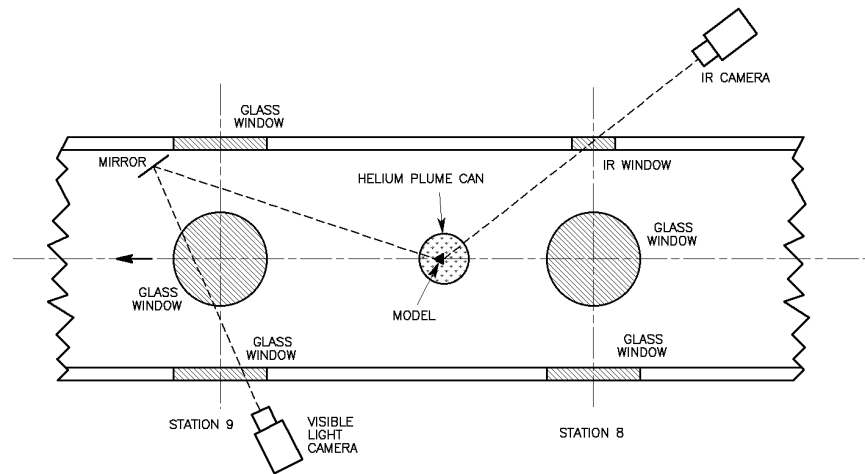

Figure 9. Top view of IR camera and helium plume set-up for forebody (at station 9) and afterbody (at station 8) heat flux measurements. Set-up number 1. Small helium can.
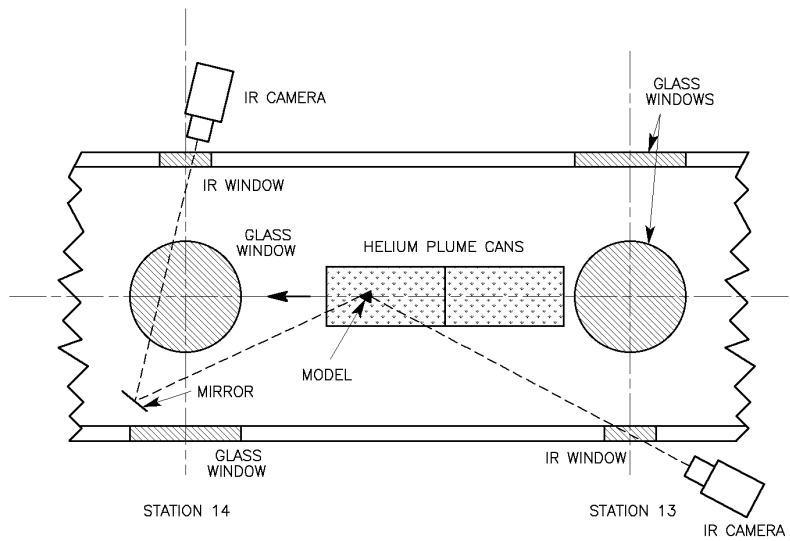
Figure 10. Top view of IR camera and helium plume set-up for forebody (at station 14) and afterbody (at station 13) heat flux measurements. Set-up number 2. Extended helium can.
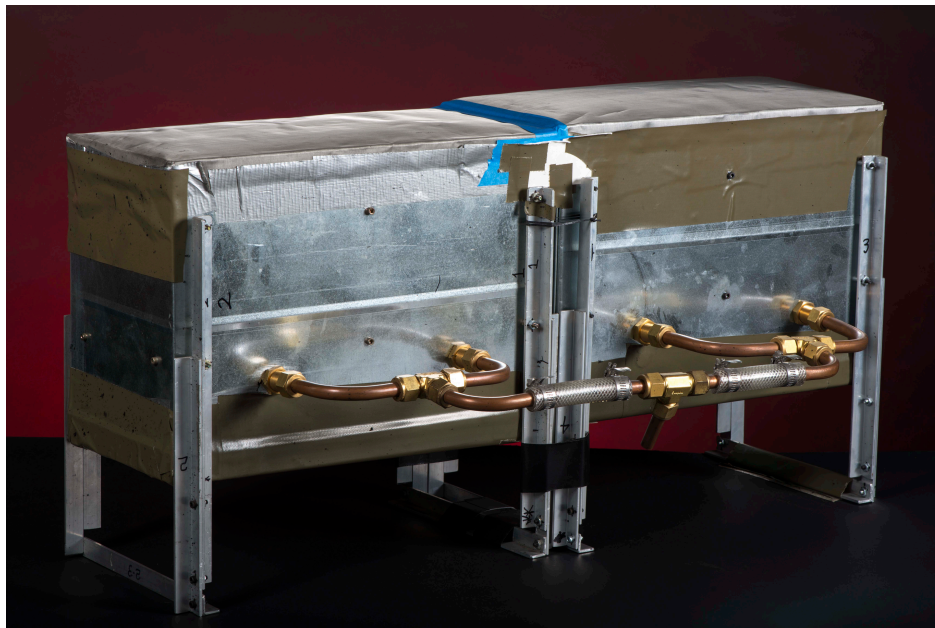

Figure 11. Photo of helium cans (extended can) used for heat flux measurements.

V. MODELS AND TEST CONDITIONS

Figure 12 shows sectional drawings of the two models used in the current study. The models are not drawn to the same scale. The left model is a 1.588 cm diameter Ti-6Al-4V titanium alloy or 304 stainless steel sphere. The right model is a 3.302 cm diameter Ti-6Al-4V titanium alloy 45 degree sphere-cone with a 0.76 cm nose radius. Both models have a Vespel insert in the rear. The sphere-cone model has an aluminum rear stud into which the Vespel insert is placed.
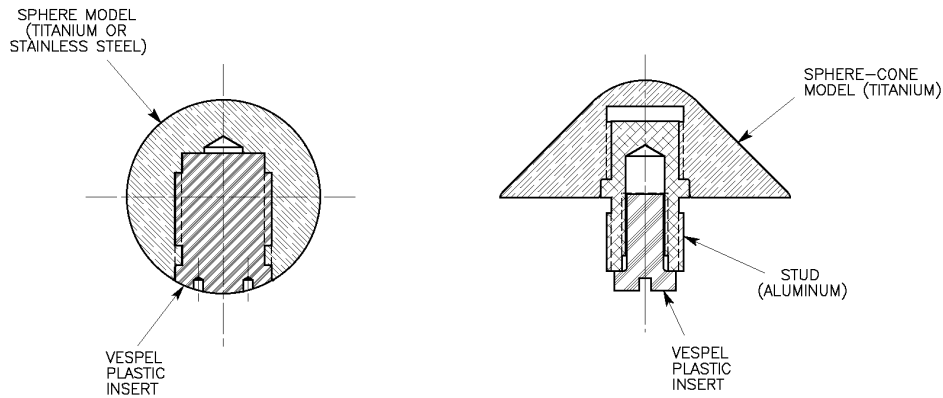

Figure 12. Sphere (left) and 45 degree sphere-cone (right) models. Models are not drawn to the same scale.

Figure 13 shows (a) a photo of the sphere model and (b) the model with its launch sabot. The sabot comprises 4 serrated fingers and an obturator disc to prevent the drive gases in the gun barrel from passing through the joints between the sabot fingers and creating thermal imprints on the rear of the model. In Fig. 13(b), to the left and right are seen single sabot fingers. In the center are seen two sabot fingers assembled around the model and sitting on top of the obturator disc. The Vespel insert can be seen in the bottom of the model in Fig. 13(b).

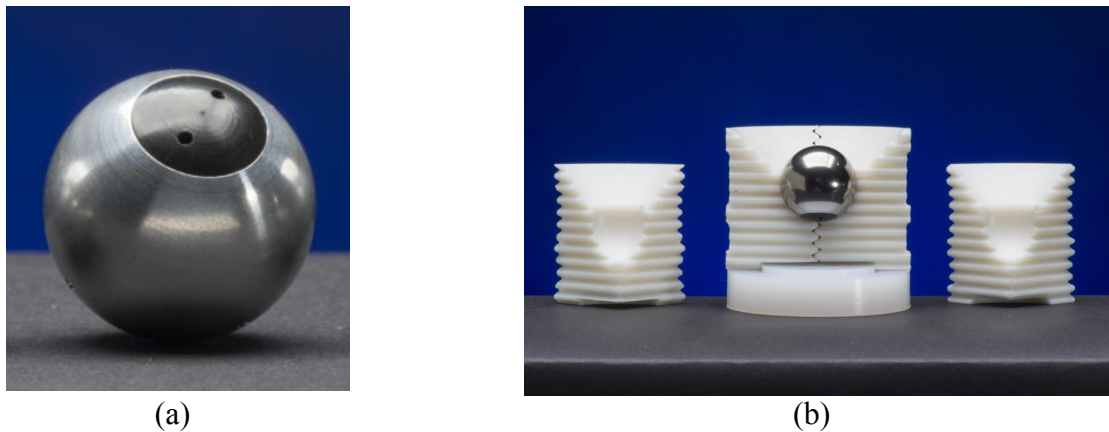(a)   (b)

Figure 13. (a) Sphere model and (b) model with launch sabot fingers (4) and obturator disc.

Figure 14 shows a sphere-cone model, the aluminum rear stud and the Vespel insert. The nose of sphere-cone model has been bead blasted, while the cone surface is smooth. Figure 15 shows an assembled sphere-cone model sitting inside of three sabot fingers, which are, in turn, resting on the obturator disc. A single sabot finger is shown lying down to the right. This is the launch configuration for the sphere-cone models in the present study. However, the assembled model shown in Fig. 15 is an earlier model with a different finish and without the Vespel insert.

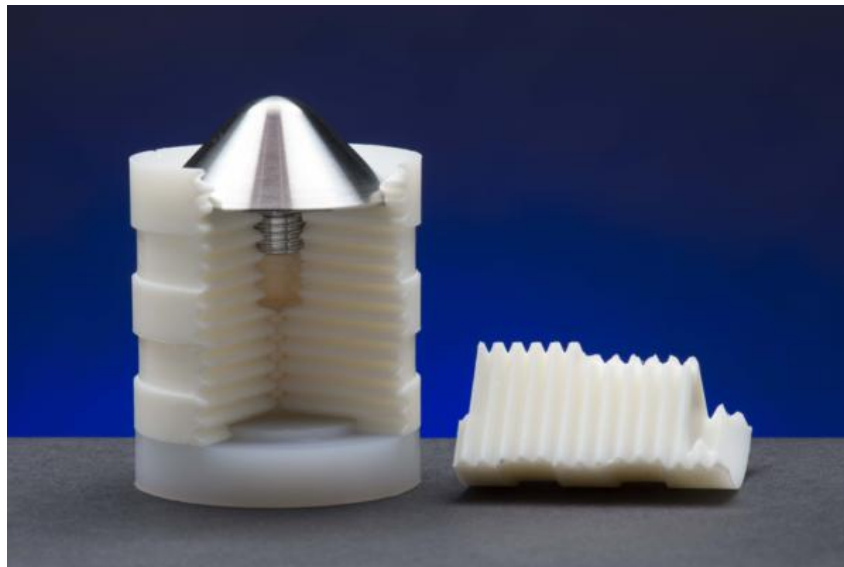Figure 14. Sphere-cone model, aluminum rear stud and Vespel insert.

Figure 15. Sphere-cone model sitting within three fingers of the launch sabot, which are, in turn, resting on the obturator disc. One finger of the sabot is seen lying down to the right

The nominal test conditions are given in Table 2 below.

Table 2. Nominal test conditions.

Model	Model material	Nominal mid-range velocity (km/s)	Test gas	Test gas pressure (Torr)
1.588 cm diameter sphere	304 stainless steel	4.76	CO_2	76
3.302 cm diameter 45 degree sphere-cone with 0.762 cm nose radius	Ti-6Al-4V titanium alloy	2.70	CO_2	76

VI. IR PICTURE DATA

Figure 16 shows an afterbody IR picture for shot 2715. This shot had a stainless steel hemisphere model launched at 5.00 km/s in 76 Torr CO_2. (We note that this is not one of the models or test conditions for which heat flux data is given herein.) The photo views the rear of the model, with camera off to one side and a viewing angle of $30 - 45$ degrees. At the left side of the model is seen a narrow crescent of the hot forebody. The remainder of the light comes from the wake extending off the afterbody. Only one of the two helium plume cans seen in Figs. 10 - 11 was used. It is seen that this shorter helium plume leaves a substantial amount of radiation in the wake, which would severely compromise the measurement of the afterbody temperatures and heat fluxes. (Much of the wake image seen in Fig. 16 is in the saturation range of the camera.) Figure 17 shows an afterbody IR picture for shot 2720, with an identical model at the same range condition as for shot 2715, but using both helium plume cans. It is seen that the wake radiation (to the right of the hot forebody crescent) has been nearly eliminated. Hence, the decision was made to use the two helium plume cans seen in Figs. $10 - 11$ (if notch filters were not used).
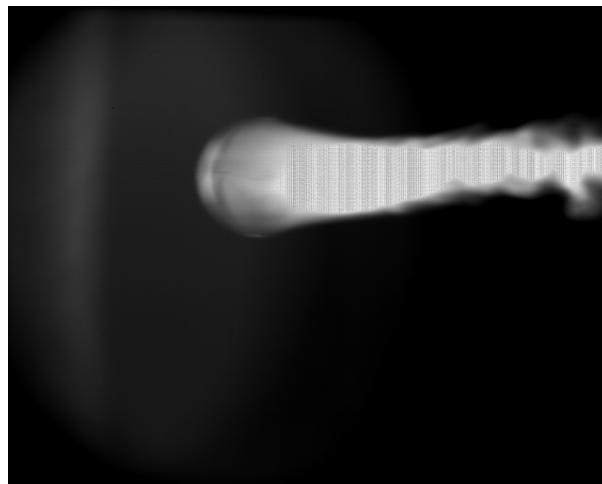

Figure 16. Afterbody IR picture for shot 2715. Stainless steel hemisphere at nominal test condition of 5 km/s in 76 Torr CO_2. Only one of the two helium plume cans seen in Figs. 10 - 11 was used for this shot.

Figure 17. Afterbody IR picture for shot 2720. Stainless steel hemisphere at nominal test condition of 5 km/sec in 76 Torr CO_2. Both helium plume cans seen in Figs. 10 - 11 were used for this shot.

Figure 18 shows the afterbody IR picture for shot 2717 at station 13 in the ballistic range. This shot was with the titanium 45 degree sphere-cone at the nominal test condition give in Table 1. This model had the rear aluminum stud and Vespel insert seen in Figs. 13 and 15. The camera position and viewing angle are very similar to those discussed above in connection with Figs. 16 and 17. The large ellipse is forebody radiation from the trailing edge of the cone. The small off center circle is afterbody radiation from the tip of the Vespel insert. Both helium plume cans seen in Figs. 10 - 11 were used for this shot. Figure 18 gives the raw camera count data. Figure 19 gives the temperatures in degrees Kelvin assuming an emissivity of unity for the Vespel and an emissivity of 0.3 for the titanium. The IR camera was calibrated with a black body source on the bench, but with the same optical set-up as was used in the ballistic range. The Vespel temperature is estimated to be 357 K. The camera and helium plume can setup for this data are shown in Fig. 10.

The afterbody IR picture for the stainless steel sphere model is shown in Figure 20 (shot 2766, station 8). The nominal test condition at 4.76 km/s is given in Table 1. The small helium plume can seen in Fig. 9, plus a notch filter with a 3875 - 4125 nm window were used for this shot. Figure 9 also shows the camera set-up for this shot. Figure 21 gives the temperatures in degrees Kelvin assuming an emissivity of unity for Vespel. The temperature in the center of the Vespel insert is estimated to be 586 K.
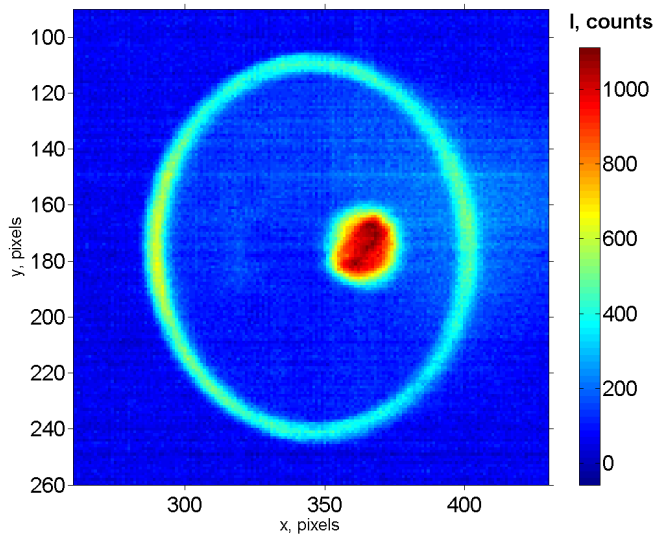
Figure 18. The afterbody IR picture at station 13 in the ballistic range for shot 2717. Titanium 45 degree sphere-cone at nominal test condition of 2.7 km/s in 76 Torr CO_2. Both helium plume cans seen in Figs. 10 - 11 were used for this shot. Picture shows raw camera count data.
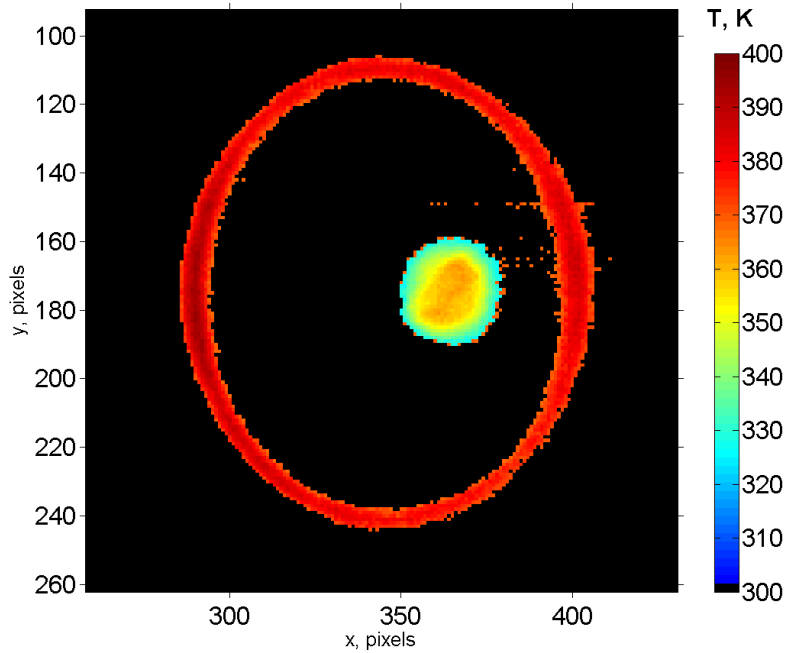

Figure 19. The afterbody IR picture at station 13 in the ballistic range for shot 2717. Titanium 45 degree sphere-cone at nominal test condition of 2.7 km/s in 76 Torr CO_2. Both helium cans seen in Figs. 10 - 11 were used for this shot. Temperatures in degrees Kelvin based on emissivities of unity for the Vespel and 0.3 for the titanium.
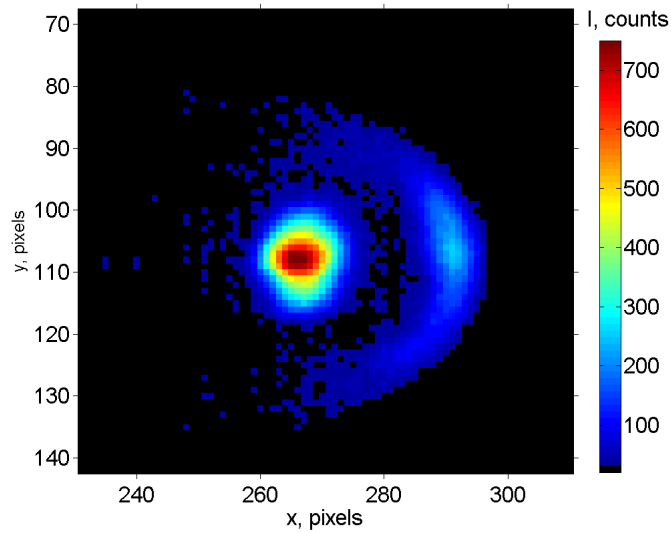
Figure 20. The afterbody IR picture at station 8 in the ballistic range for shot 2766. Stainless steel sphere at nominal test condition of 4.76 km/s in 76 Torr CO_2. The small helium can seen in Fig. 9 was used for this shot, plus a notch filter with a $3875 - 4125$ nm window. Picture shows raw camera count data.

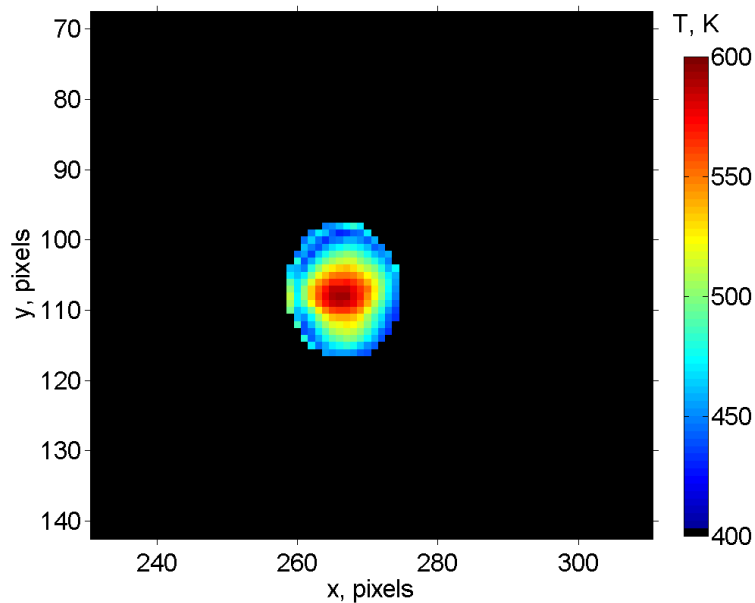Figure 21. The afterbody IR picture at station 8 in the ballistic range for shot 2766. Stainless steel sphere at nominal test condition of 4.76 km/s in 76 Torr CO_2. The small helium can seen in Fig. 9 was used for this shot, plus a notch filter with a $3875 - 4125$ nm window. Temperatures in degrees Kelvin based on emissivity of unity for Vespel. Picture has been cropped to remove area outside the Vespel insert.

For future afterbody heat flux measurements in CO_2, it may be desirable to continue to use notch filters to reduce the wake radiation. The filters may be used with helium plumes (either the small plumes seen in Figs. 2 and 9 or the extended plumes seen in Figs. 10 and 11) or without helium plumes. A number of notch filters with transmission windows set in the 3.1 – 4.1 microns range between the CO_2 emission bands peaking at 2.8 and 4.3 microns have been used with encouraging results. The filters used to date have windows of 3875 - 4125, 3440 - 4075 and 3100 - 4200 nm. As mentioned previously, the data of Figs. 20 and 21 were taken with a small helium plume and a 3875 - 4125 nm notch filter. The use of the notch filters may permit one to operate with the small helium plumes (or possibly, with no plumes at all) instead of the extended plumes. For tests in air, it is believed that the wake radiation will be much weaker than with CO_2 and will pose much less of a problem.

VII. DATA ANALYSIS

To calculate the heat fluxes on the afterbody Vespel SP-21 inserts from the measured temperatures, the Vespel thermal properties as a function of temperature must be known. Brochures and reference books only give the thermal properties of the Vespel SP-21 plastic (with 15% graphite fill) at room temperature. From data on unfilled Vespel SP-1 and graphite as a function of temperature, the thermal properties of Vespel SP-21 were estimated as described in Appendix A. These estimated thermal properties were used to calculate the experimental afterbody heat fluxes discussed below.

Figures 22 and 23 show the theoretical (CFD) and experimental heat flux values for shot 2717. This shot was a 45 degree Ti-6Al-4V sphere-cone fired at a mid-range velocity of 2.70 km/s into 76.2 Torr of CO_2. The CFD values were computed as described in Sec. III. The curved blue lines show the fore-body and part of the afterbody results at a wall temperature of 295 K. The CFD stagnation point heat flux is 1950 W/cm^2. The red line shows the afterbody results at a wall temperature of 350 K. The heavy blue horizontal lines show the experimental measurements. For the sphere-cone, hydrogen was used in the launch tube, which essentially eliminated in-barrel heating. Hence, the wall temperature for the forebody data was taken to be 295 K. For the afterbody data, the CFD calculations were made at a wall temperature of 350 K, which is very close to the value to be expected at station 8. Heat fluxes (Qs) taken at a given x-distance down the range were scaled to other x-distances using a (velocity)^3 scaling as shown in the equation below.

$$Q(x_2) = Q(x_1) \frac{[V(x_2)]^3}{[V(x_1)]^3} \qquad (5)$$

It is seen that the experimental stagnation point heat flux is about 1.5% higher than the CFD value. The experimental heat flux on the Vespel insert is seen to be about 0.51 times the CFD value. The experimental heat fluxes for the test gas were calculated by assuming the (velocity)^3 scaling of Eqn. (5) as the model moves down the range in the test gas. During the times that the model was inside a helium plume a correction Q(He)/Q(test gas) was applied. For the stagnation point heat fluxes, this ratio was calculated using the correlations of Refs. [5] and [6]. For the afterbody heat fluxes, this ratio was calculated as described in the previous paragraph for the test gas and pure helium. For the afterbody correction, since the CO_2 in the wake is progressively replaced by helium as the model travels through the helium plume (e.g, see Fig. 17 and associated discussion), the wake correction is applied assuming that the time in pure helium is half the actual value spent in the plume. For shot 2717, the afterbody correction raises the heat

flux about 9% above the value which would be calculated if no correction were to be applied. For the corresponding experimental stagnation point heat fluxes, the helium plume correction raises the heat fluxes about 13% above the values with no correction applied. The helium plume corrections have been applied for the experimental data seen in Figs. 22 and 23.
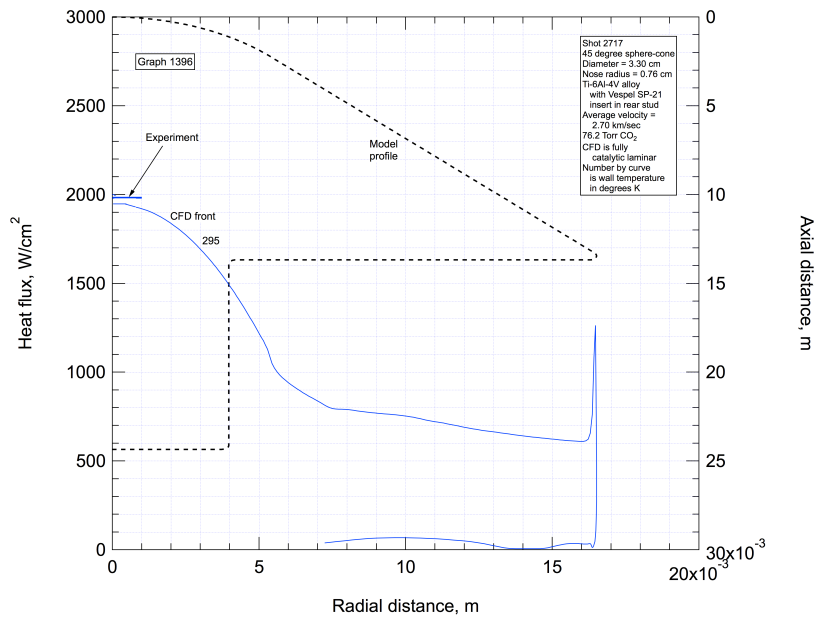

Figure 22. Experimental and CFD forebody heat fluxes for Ti-6Al-4V 45 degree sphere-cone at a mid-range velocity of 2.70 km/s. Test gas in 76.2 Torr CO_2.
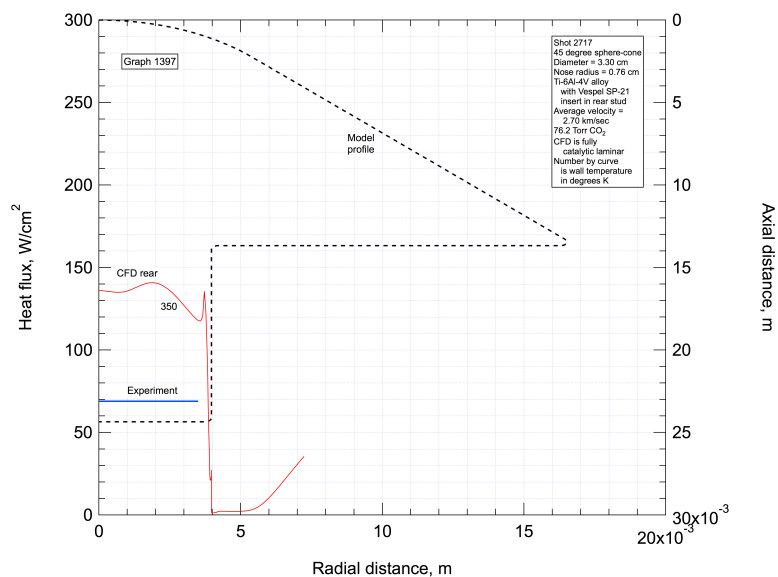

Figure 23. Experimental and CFD afterbody heat fluxes for Ti-6Al-4V 45 degree sphere-cone at a mid-range velocity of 2.70 km/s. Test gas in 76.2 Torr CO_2.

Figures 24 and 25 show the predictive (CFD) and experimental heat flux values for shot 2766. Shot 2766 was a 304 stainless steel sphere fired at a mid-range velocity of 4.76 km/s into 76.0 Torr of CO_2. Again, the CFD values were computed for laminar flow, a fully catalytic wall condition and with an 8 species chemistry model. The purple lines show the fore-body results at

a wall temperature of 1020 K, the measured value at station 13. Again, heat fluxes taken at a given x-distance down the range were scaled to other x-distances using a (velocity)^3 scaling. The CFD stagnation point heat flux scaled to station 8 is 7380 W/cm^2. The heavy blue horizontal line shows the experimental measurements. For this model, hydrogen was not used in the launch tube. Thus, there was substantial in-barrel heating. Based on previous results for similar conditions, an in-barrel heating rate of 6320 W/cm^2 lasting over the time for the model to traverse the length of the barrel at the full muzzle velocity was assumed. The stagnation point wall temperature at the muzzle was estimated to be 660 K. For the afterbody data, the CFD calculations were made at a wall temperature of 586 K, the measured value at station 8. The CFD heat flux at the center of the Vespel insert is 566 W/cm^2.

It is seen that the experimental stagnation point heat flux is about 1% lower than the CFD value. The experimental heat flux on the Vespel insert is seen to be essentially identical the CFD value. This excellent agreement is likely fortuitous, since the accuracy of the afterbody experimental heat flux measurements is estimated to be the same as that for the forebody heat flux measurement technique, which was given to be ±10% in Ref. 1. For shot 2766, the afterbody correction raises the heat flux about 3% above the value which would be calculated if no correction were to be applied. This value is lower than for shot 2717, since the model run in helium is much less for shot 2766 (see Fig. 9) than for shot 2717 (see Fig. 10). For the corresponding experimental stagnation point heat fluxes, the helium plume correction raises the heat fluxes about 18% above the values with no correction applied. The helium plume corrections have been applied for the experimental data seen in Figs. 24 and 25.
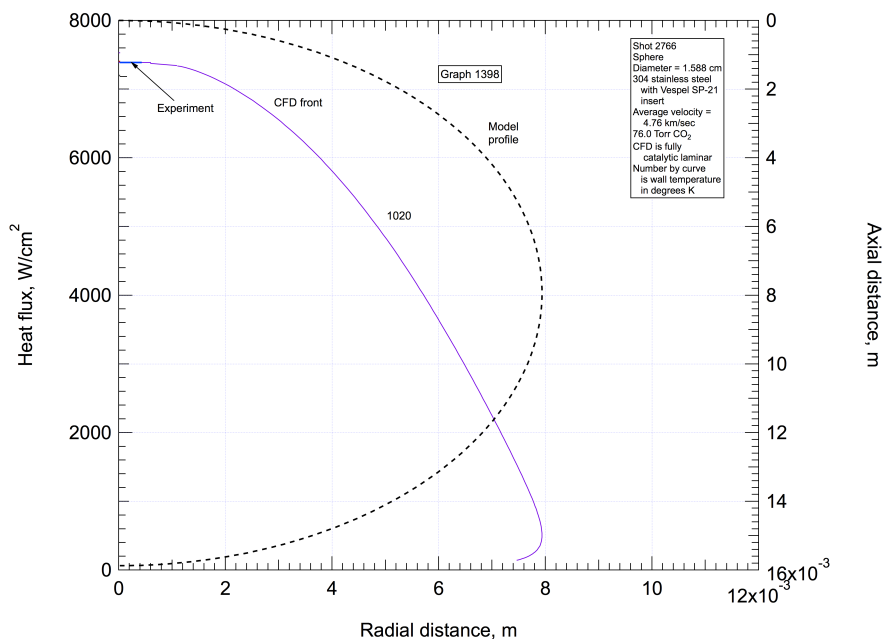

Figure 24. Experimental and CFD forebody heat fluxes for 304 stainless steel sphere at a mid-range velocity of 4.76 km/s. Test gas in 76.0 Torr CO$_2$.
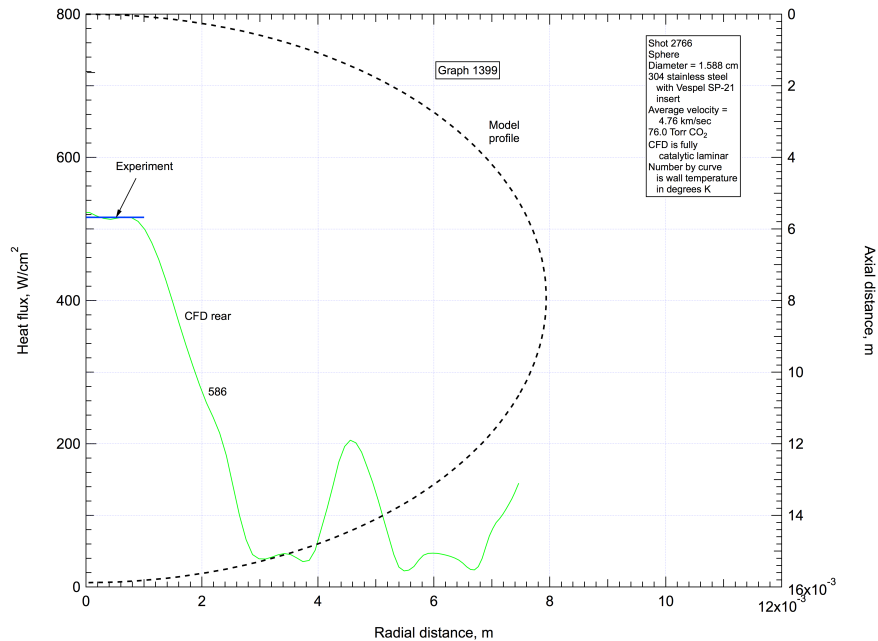
Figure 25. Experimental and CFD afterbody heat fluxes for 304 stainless steel sphere at a mid-range velocity of 4.76 km/s. Test gas in 76.0 Torr CO_2.

The experimental stagnation point heat fluxes for both models were within 1.5% of the CFD values. For the sphere model, the experimental heat flux on the afterbody Vespel insert is seen to be within 1% of the CFD value. By contrast, for the sphere-cone model with the aft stud, the experimental heat flux on the Vespel insert at the end of the stud is only 51% of the CFD value.

   There are several possible reasons for this difference. Unsteady wake flows are particularly difficult to model. The shadowgraphs show unsteadiness in the wake region, whereas the CFD calculations (as modeled here) are completely steady. Further, the model is pitching and yawing somewhat, whereas the CFD calculations are for zero angle of attack in pitch and yaw. The pitch and yaw angles are 1 − 1.5 degrees in the first half of the range and increase to 2 − 3 degrees in the second half of the range. Reference 7 show large reductions in the CFD calculated heat fluxes at the tip of the afterbody of an entry vehicle for angles of attack of 0.5 − 2.0 degrees (when compared to the calculated heat fluxes at exactly zero angle of attack). Also, the CFD modeled OML (outer mold line) (see Figs. 22 and 23) does not capture all of the details of the actual range model (see Fig. 12). This includes threads, diameter steps and the screwdriver slot.

   For the sphere, the situation is different. One would expect the flow over the sphere to be essentially unchanged at pitch and yaw angles of attack. Also, the OML of the CFD model of the sphere is identical with OML of the actual range model except for the small spanner wrench holes.

VIII. SUMMARY AND CONCLUSIONS

   A proven technique for measuring the heat fluxes over model forebodies in the ballistic range was described.   The modifications of this technique needed to make afterbody heat flux measurements was given. This involved the use of an extended helium gas plume and/or filters to remove the glowing wake and the use of special high conductivity, high temperature capability graphite-filled plastic for the afterbody.   The models and test conditions were described. Raw data in the form of model surface temperature plots were presented. Finally, experimental and CFD heat flux data for forebody and afterbody heat fluxes were presented and compared. Data were presented for a 45 degree sphere-cone (with a projecting rear stud) at 2.70

km/s and for a sphere at 4.76 km/s. Both models were launched into 76 Torr of CO_2 gas. The experimental forebody heat fluxes were within 1.5% of the CFD values, whereas the experimental afterbody heat fluxes were within 1% of the CFD values for the sphere, but only 51% of the CFD value for the sphere-cone with an aft protruding stud.

The technique appears to be very promising to allow one to measure afterbody heat fluxes for proposed entry vehicles in the ballistic range. With this data obtained at relatively very low cost in a ground test facility, one could design afterbody heat shields with smaller safety margins, hence leading to lighter heat shields and increased science payloads. With data from only two piggyback test shots, these conclusions must, at this time, be regarded as preliminary. More shots are planned in the near future to increase the database of the technique.

APPENDIX A

In this appendix, we discuss the technique used to estimate the thermal properties of Vespel SP-21 with 15% graphite fill as a function of temperature. Brochures and reference books only give the thermal properties of the Vespel SP-21 plastic at room temperature. From data on unfilled Vespel SP-1 and graphite as a function of temperature, the thermal properties of Vespel SP-21 were estimated as described below. Reference [8] gives the thermal properties (thermal conductivity and specific heat) of the unfilled Vespel SP1 from 0 to 300 C. Both properties are seen to vary nearly linearly with temperature. These thermal properties were then linearly extrapolated to 500 C. It is noted that the extrapolated values will not actually be used in the analyses all the way to 500 C since there are temperature limits for the filled Vespel SP-21. References [9] and [10] give a heat deflection temperature of 360 C at 264 psi pressure and Ref. [9] gives a maximum continuous use temperature of 427 C.

Reference [11] gives specific heat data for POCO graphite over the temperature range 300 – 2400 K. We use only the values from 0 to 500 C. For simplicity, a linear fit was used for the specific heat data, although the slope of the actual curve decreases with temperature. The maximum errors in the specific heat values of graphite caused by using the linear fit are 5 – 7%, but when applied to the Vespel SP-21 with 15% of graphite fill, the maximum errors for the Vespel are about 2%. Reference [12] gives thermal conductivity values over a wide temperature for number of extruded graphites and pyrolytic graphite. The curve for Acheson graphite was roughly in the middle of the curves for extruded graphites. The curve for the pyrolytic graphite was quite different. Hence, to estimate the thermal conductivity of the Vespel SP-21, two sets of conductivity values for graphite were used – one for Acheson graphite and the other for pyrolytic graphite. For the Acheson graphite, the values parallel to the axis of extrusion were roughly 1.35 times those normal to the axis of extrusion and an arithmetic mean value was used. For the pyrolytic graphite, the values parallel to the layer planes were roughly 340 times those perpendicular to the layer planes and a geometric mean value was used. The averaged values for the Acheson graphite range from 1.24 to 2.1 times those for the pyrolytic graphite.

Several models for the graphite fill and unfilled Vespel SP-1 were tried to attempt to match the measured conductivity of the filled Vespel SP-21 at room temperature. In one model, the graphite was considered to be solid plates aligned parallel to the heat flow direction. This gave a thermal conductivity roughly 20 times the measured value. In a second model, the graphite was considered to be solid plates aligned normal to the heat flow direction. This gave a thermal conductivity roughly half the measured value. Finally, a model was constructed with one cube with the graphite plates aligned parallel to the heat direction on top of a second cube with the graphite plates aligned normal to the heat flow direction, the heat flowing through the two cubes in series. This gave a thermal conductivity fairly close to, but not exactly equal to, the true value. An adjustment (away from the true value) was made to the relative volume occupied by the graphite and the Vespel SP-1 to bring the modeled conductivity into exact agreement with the measured conductivity at room temperature. Finally, this structural model was used with the measured (or extrapolated) values of conductivities of the graphites and the Vespel SP-1 at various temperatures to estimate the thermal conductivity of the Vespel SP-21 over the temperature range 0 to 500 C. The difference between the estimated thermal conductivities of the Vespel SP-21 at 500 C based on the two different graphites was not large, about 4%. For the analyses herein, the estimated thermal conductivity of Vespel SP-21 was based on the thermal conductivity of the Acheson graphite. The specific heat values of the Vespel SP-21 were estimated by simply taking 15% of the values for POCO graphite plus 85% of the values for the Vespel SP-1. The estimated values of both the specific heat and the thermal conductivity of the Vespel SP-21 increase nearly linearly with temperature over the range 0 to 500 C.

REFERENCES

1. M. J. Wright, R. A. S. Beck, K. T. Edquist, D. Driver, S. A. Sepka, E. M. Slimko, W. H. Willcockson, A. DeCaro and H. H. Hwang, "Sizing and Margins Assessment of the Mars Science Laboratory Aeroshell Thermal Protection System," Paper AIAA 2009-4231, Presented at the 41st AIAA Thermophysics Conference, San Antonio, Texas, 22 – 25 June, 2009.
2. M. C. Wilder, D. C. Reda and D. K. Prabhu, D. K., "Heat-transfer measurements on hemispheres in hypersonic flight through air and CO_2," AIAA paper 2011-3476, 42nd AIAA Thermophysics Conference, 27 – 30 June 2011, Honolulu, Hawaii.
3. M. J. Wright, T. White and N. Mangini, "Data-parallel line relaxation methods (DPLR) code user manual Acadia-version 4.01.1," NASA/TM-2009-215388, Oct. 2009.
4. J. P. Holman, "Heat Transfer," 6th ed., McGraw-Hill, New York, 1986, Fig. 4-4, p. 137.
5. E. V. Zoby, "Empirical stagnation-point heat-transfer relation in several gas mixtures at high enthalpy levels," NASA TN D-4799, October, 1968.
6. K. Sutton and R. A. Graves, Jr., "A general stagnation-point convective-heating equation for arbitrary gas mixtures," NASA TR R-376, November, 1971.
7. R. D. McDaniel, M. J. Wright and J. T. Songer, "Aeroheating Predictions for Phoenix Entry Vehicle," Journal of Spacecraft and Rockets, Vol. 48, No. 5, Sept. – Oct. 2011, p. 741 (Fig. 24b), p. 742, (Fig. 26b).
8. R. A. Jacobs-Fedore and D. E. Stroe, "Thermophysical properties of Vespel SP-1," in *Thermal Conductivity 27*, Proceedings of the 27th International Thermal Conductivity Conference, 2003, Knoxville, TN, H. Wang, W. D. Porter and G. Worley, eds., Lancaster, PE: DEStech Publications, pp. 231 – 238.
9. *Machine Design*, December, 1993, p. 128.
10. DuPont company, brochure on properties of Vespel SP-21.
11. C. Y. Ho, R. W. Powell and P. E. Liley, "Thermal conductivity of the elements: A

comprehensive review," *Journal of Physical and Chemical Reference Data*, **3**, 1974, Supplement, No. 1, pp. 127 – 172.

12. R. E. Taylor and H. Groot, "Thermophysical properties of POCO graphite," *High Temperatures – High Pressures,* **12**, 1980, pp. 147 – 160.